Mathematical morphology-based point cloud analysis techniques for geometry assessment of 3D printed concrete elements

Sooraj A. O. Nair[1], Gaurav Sant[2], Narayanan Neithalath[3]

Abstract

In 3D printing of cement-based materials, it is imperative to ensure geometrical consistency of the print with the as-designed/modeled system. Time-dependent, deformable systems like concrete present multiple challenges in ensuring appropriate post-print quality. This paper presents a suite of point cloud comparison techniques, which can be used individually or in combination, to quantify the amount of mismatch between the as-designed and as-printed systems, using morphological analysis. A semi-quantitative error distance method is proposed, which can be easily accomplished using direct mapping of the actual and reference point clouds. A print accuracy index (PAI) based on centroidal distances is proposed as a global quantifier of the print quality. Furthermore, a topological set theory (TST)-based approach is used to determine layer-wise overlap, which helps in isolating localized inconsistencies. The methods are tested on a variety of small cuboids, and further verified using a larger mortar print. It is expected that these methodologies can be suitably adapted to indicate the efficiency of the print, after the fact, or during printing. The latter facilitates in-line quality checks, that can in turn lead to real-time alterations in the materials or processes.

Keywords: 3D printed concrete; Point cloud analysis; Print accuracy index; Error distance; Mathematical morphology; Quality control

---

[1] Graduate student, School of Sustainable Engineering and Built Environment, Arizona State University, Tempe AZ 85287

[2] Professor and Henry Samueli Fellow, Department of Civil and Environmental Engineering, University of California Los Angeles, Los Angeles CA 90095

[3] Professor, School of Sustainable Engineering and Built Environment, Arizona State University, Tempe AZ 85287; Corresponding Author (Phone: +1-480-965-6023; Fax: +1-480965-0557; e-mail: Narayanan.Neithalath@asu.edu)

1 Introduction

3D printing of concrete is an additive manufacturing technology that enables automated construction of buildings in a faster, cheaper, and sustainable manner [1,2]. Layer-wise extrusion is the most common 3D printing method for concrete [3,4]. Successful extrusion of cementitious binders, and its buildability (ability to build up successive layers without exaggerated deformation and loss of stability in the fresh state) are important attributes in concrete 3D printing, which are dependent on the material rheology, time-dependent property development, and the printing process [5,6]. It has been shown that the shaping and frictional stresses during extrusion, and the geometry of the extruder influences the evolution of particle packing and liquid filtration that impacts smooth and defect-free extrusion of the material [7,8]. Once extruded, the buildability of the system depends on the evolution of fresh properties, interlayer properties, and the printing process parameters including the time delay between successive layer printing [9–11]. It is thus evident that the quality of the printed structure in the hardened state is a function of the fresh properties of the mixture, the extrusion parameters, and the type of printer used. The process continuum in Figure 1 shows the properties of interest during and after printing, along with the characteristics relevant to the printing process. As has been elucidated in several recent works, printability and shape retention of the mixture in the fresh state, which translates to dimensional accuracy with respect to the design in the hardened state, are functions of the yield stress and thixotropy of the material [12–14]. In-line quantification of extrudability has been reported as a quality control technique for 3D printed concrete [15]. In general, the post-print characterization of 3D printed systems are carried out in terms of the hardened mechanical properties, i.e., compressive and flexural strengths determined with considerations of directional anisotropy of the printed structure [16,17], including real-time quantifications [18]. However, efforts to evaluate the surface quality and precision, which are influenced by a large array of factors in concrete 3D printing, have been limited.

The sequential layering of the material, and the fact that the fresh concrete is bound to deform under self-weight and imposed loading, creates variability in surface profiles, including what is commonly referred to as the staircase effect [19–21]. Minor variations in surface profile, while architecturally not desirable, might not be structurally detrimental, especially in the construction of walls. However, when 3D printed concrete is used in the fabrication of bespoke elements, dimensional accuracy and tolerances are critical. Some 3D concrete printers are equipped with trowels to ensure finished surfaces, providing improved tolerances [22]. There are several variables that influence the surface profile of a printed concrete element. They include (but are not limited to) layer height, filament size and shape, print path, material flow rate, material rheology

(influenced by mixture design), process time, and volume changes during setting and hardening. To ensure a sufficient level of post-print quality, the surface profile of the 3D printed element can be compared to that of the design input. As shown in Figure 1, a short-term (immediate) analysis can help in establishing a quality control procedure based on surface profile analysis, and refine the parameters related to printing described earlier.

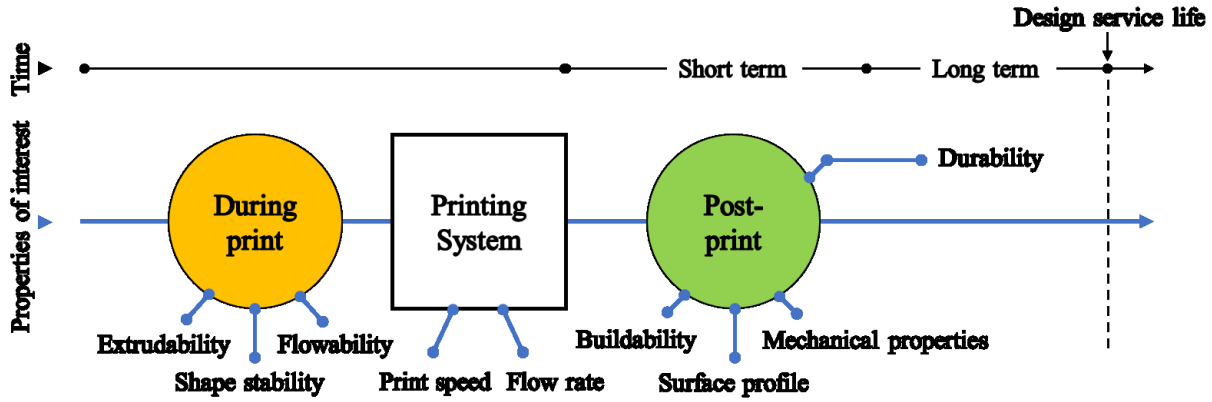

Figure 1: The process continuum in 3D printing with the parameters that are important at different times.

3D model data is generally represented and saved as an array of cartesian co-ordinate data that constitutes the spatial positioning and surface (or volume) generation of the model, known as a *point-clouds*. These datasets define the three dimensional location, shape, and color of the model saved in various ASCII formats including '.xyz', '.ptx', and '.obj'. To generate the point cloud data to be used for geometrical analysis in prototypes before mass production, 3D scanners can be used. Such information is beneficially used in building information modeling (BIM) processes in construction. The process of 3D scanning and subsequent printing or reconstruction (using different printing methods) have been successfully employed in several engineering applications including architectural reconstruction and biomedical applications [23,24]. Point cloud data acquisition techniques have been used to acquire post-print surface profiles, which are then analyzed for conformance to the design model [25,26]. Octree comparison and cloud mapping techniques have been used to develop measures to qualify and quantify the output print quality [27]. The Iterative Closest Point (ICP) algorithm compares and predicts the closeness of a set of points of interest based on Hausdorff distance [28,29]. This technique is widely used in matching a pair of point clouds using specific topological information. Specific to concrete 3D printing, the surface profile depends on the rheological (static yield stress, viscosity, thixotropy, and rate of setting of the mixture), extrusion (pressure

and flow rate), and print-related (nozzle diameter, filament dimensions, and print speed) parameters as described earlier. Several non-contact techniques have been used to assess the fresh-state surface profiles and deformations during printing. Computer vision has been used to predict the extrusion rate of filaments using a coupled camera–nozzle system to determine under- or over-flow during extrusion [30]. The filament quality in terms of expected-to-actual filament flow have also been quantified using indices like solidity ratio, shape retention factor, and flow ratio [12,31,32]. Small-scale prints or segments of a larger print could be scanned using compact scanners to extract the surface profiles of the print. A 3D structured light scanning system has been used for scanning, along with characterization of the geometry using degree of distortion, surface roughness, and area deficiency [33]. Geometric dimensioning and tolerancing employed in traditional manufacturing processes have also been used to understand the effects of nozzle and layer dimensions on the overall print quality [19]. A more convenient printability index based on Hausdorff distances has been shown to quantify the suitability of the print medium, and relate the mixture characteristics to the print output quality [34,35]. Some of these methods employ point cloud comparison and derive parameters to define the print quality, while others employ image analysis and direct filament measurements as tools to evaluate the output filament quality.

This paper puts forward analysis techniques based on fundamental concepts in point-set topology, coupled with acquired point data clouds to develop a robust surface profile quantification, that can be used for quality control during or immediately after printing of cement-based materials. In this work, we propose a two-level procedure for print output qualification, in terms of geometrical tolerances. The method is based on using a global and segmental (layer-wise) point cloud analysis. Level 1 analysis evaluates several scans of printed specimens subjected to conventional visual point cloud comparison methods to quantify the mismatch of the printed output to the design file. Level 2 analysis uses extended quantification of the print quality using a unique print accuracy index based on centroidal distances, and a topological set theory-based surface comparison using reduced scan data. The modified set theory approach considers extended relations between data sets [36]. The combined approach is used to establish a quality control test procedure for in-situ post-print qualification.

2 Experiments and Analysis Methods

2.1 Materials and mixtures

Ordinary portland cement (OPC; conforming to ASTM C 150), fine limestone powder (L; conforming to ASTM C 568), microsilica (M; conforming to ASTM C 1240), and metakaolin (K; conforming to ASTM

C 618) were used to proportion the pastes. The chemical compositions of the starting materials are shown in Table 1 and the mixture proportions of several paste mixtures are shown in Table 2. These proportions were selected such that the pastes were capable of being uniformly and homogeneously extruded. A detailed study on the rheological and extrusion characteristics of these mixtures were presented in an earlier work [5], and the important properties are reported in Table 2. In the acronyms for mixture identification, the letters denote the material used as cement replacement (see Table 1) and the numbers in subscripts correspond to the levels (by mass) at which they replace cement. A polycarboxylic ether based superplasticizer (suffix -s in Table 2) was used in several mixtures. The powders were dry-mixed, followed by wet mixing for 5 minutes, in a laboratory mixer.

Table 1: Chemical composition and surface areas of the paste components

Components of the binders	Chemical composition (% by mass)							BET specific surface area (m^2/kg)
	SiO2	Al_2O_3	Fe_2O_3	CaO	MgO	SO_3	LOI	
OPC	19.60	4.09	3.39	63.21	3.37	3.17	2.54	1,318
Metakaolin (K)	51.70	43.20	0.50	-	-	-	0.16	14,915
Micro silica (M)	> 90.0	-	-	< 1.0	-	-	-	18,253
Limestone (L), 1.5 µm	$CaCO_3$ > 99%							7,518

Table 2: Binder combinations and proportions for the chosen mixtures

Mixture ID	Mass fraction of ingredients				Water-to-powder ratio (w/p)	Superpl-asticizer (% by mass of powder)	Shear Stress (Pa)	Plastic Viscosity (Pa.s)
	OPC	Limestone (L); d_{50} = 1.5 µm	Micro silica (M)	Metakaolin (K)				
L_{30}	0.70	0.30	0	0	0.41	0	155.97	2.94
$M_{10}L_{20}$	0.70	0.20	0.10	0	0.435	0	159.33	2.39
$M_{15}L_{15}$	0.70	0.15	0.15	0	0.445	0	191.30	2.71
$M_5K_5L_{20}$	0.70	0.20	0.05	0.05	0.46	0	243.07	3.67
L_{30}-s	0.70	0.30	0	0	0.35	0.25	312.53	4.35
$M_{10}L_{20}$-s	0.70	0.20	0.10	0	0.35	0.45	270.09	3.30
$M_{15}L_{15}$-s	0.70	0.15	0.15	0	0.35	0.55	386.41	4.68
$M_5K_5L_{20}$-s	0.70	0.20	0.05	0.05	0.35	0.55	367.60	4.67

2.2 3D printing and scanning of cement pastes

A BCN-3D printer with a maximum allowable print dimensions of 210 × 300 × 210 mm was used in this study. The print head movement along the orthogonal axes (X, Y, Z) is assisted by stepper motors. A detachable, stepper-controlled ram extruder (100 cm^3 volume) was mounted on the print head for controlled

material feed. Hollow cuboidal samples 45 × 45 × 30 mm in size were printed through an extruder having a nozzle diameter of 4 mm. Filaments, 3 mm high and 6 mm wide, were printed at a nozzle travel speed of 20 mm/s, up to a total of 10 layers. A typical print design and a printed sample (using the L_{30} mixture from Table 2) are shown in Figure 3(a) and (b) respectively. The samples were printed within 10 minutes of mixing and cured in a moist environment for 24 h. In addition, reference samples were printed to compare with the extrusion printed specimen as shown in Figure 3(c) to 2(e). Figure 3(c) shows a fused deposition model (FDM) print of similar dimensions using polylactic acid (PLA; thermoplastic polymer) filaments (0.75 mm diameter) with a layer height of 0.2 mm, layer width of 0.4 mm, and nozzle travel speed of 30 mm/s. Figure 3(d) shows an L_{30} paste (similar to those in Figures 2(a) and (b)) printed using a Deltabot printer equipped with a screw extruder (as opposed to ram extruder for the other pastes), with a layer height of 3 mm, layer width of 6 mm, and a nozzle travel speed of 20 mm/s. Note that the PLA and deltabot print data are used even though the material, nozzle and layer dimensions, and printer type are different, to demonstrate the differences in post-print quality and geometric tolerances. Figure 3(e) shows a failed print of the L_{30} mixture due to structural instability. In real-world construction printing, mortars or concrete are used, which display better shape retention in the fresh state than cement pastes (because of the presence of stiffer aggregates). Paste specimens are used in this work to ensure that exaggerated deviations from the 3D model sometimes exist in the printed sample, to properly analyze the efficiency of the point cloud comparison techniques.

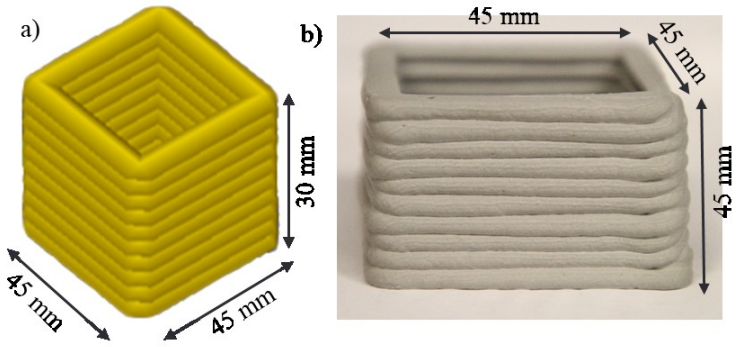

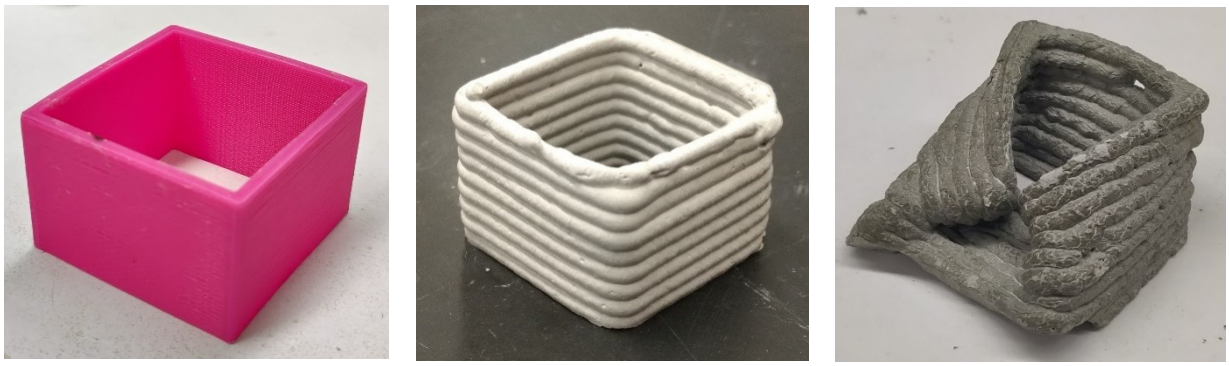

(c) (d) (e)

Figure 2: Layered cuboidal elements of size 45 × 45 × 30 mm: (a) layered design view in Slic3r© software, (b) typical printed sample using a paste mixture in a desktop cartesian printer mounted with a ram extruder, (c) FDM printed cuboid with PLA filament, (d) 3D printed cuboid using a deltabot printer mounted with screw extruder, and (e) a failed specimen due to lack of buildability. Note that cases (c) – (e) are reference cases for comparison with the extrusion printed samples.

The samples scanned using a desktop 3D Scanner as shown in Figure 4. The scanner is equipped with a high-definition camera supported by dual lasers that helps in laser triangulation of points in 3D space. The sample stage constitutes a turntable of 150 mm diameter above which the specimen is placed. A black background is placed to create contrast between the specimen and the environment for better scan output. The scanner can take models up to a height of 300 mm with a scan resolution of 0.25 mm and a rotational step resolution of 0.25º. The data acquisition software is used to execute the scan and import the raw cartesian coordinate data. The noise in the scanned data is cleaned using coarse and fine filters by radial threshold distance detection of discontinuous points. The filtered point cloud data is saved as ASCII format (.xyz or .ptx) with a typical cloud sample size of 170,000 points with around 83,000 to 86,000 points per scan step.

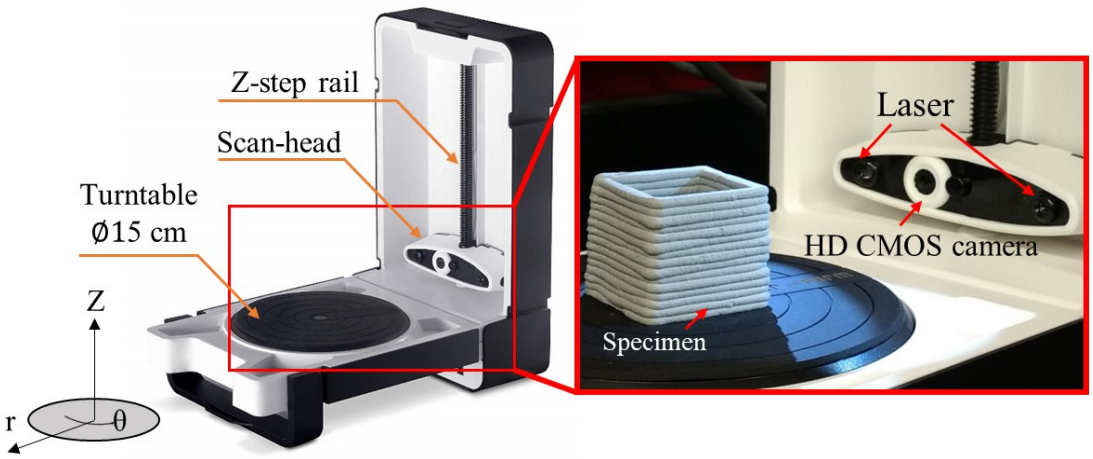

Figure 3: Desktop 3D scanner with components marked and a printed sample mounted and illuminated on the sample stage while scanning

2.3 Point cloud analysis

A 3D object can be mathematically and computationally represented as a set of cartesian co-ordinate 'point-cloud' data acquired using 3D scanners, as explained earlier. The scanned cloud data is used to compute the mismatch with the design file by using several point cloud analysis techniques as discussed in this paper. The quantification approaches utilize mathematical morphology to process the geometrical structures. A reference hollow cuboid design file (wall thickness of 0.03 mm) is used as a surface mesh format. The mesh was converted into a point cloud data generated by sampling 200,000 points for cloud-to-cloud alignment and distance measurements.

2.3.1 Error distance distribution

This approach uses an open-source software, Cloudcompare™ to carry out the analysis and compare the output cloud with the reference point cloud data. The software inputs the scanned point cloud data along with the reference mesh, followed by transformations and point-cloud alignment as shown in Figure 4. The outlier points are removed by segmentation and noise filters. The mesh and cloud are coarse-aligned using 'point pairs picking' to select pairs of similar points in both the clouds for at least three points to orient the data. The alignment was restrained to the necessary boundary condition that the base planes (Z=0) should align. This is followed by fine registration of the scanned cloud using the iterative closest point (ICP) algorithm [29] to fine-register the position of the scanned cloud over the reference mesh. Both coarse and fine alignment involves translational and rotational transformation of the coordinate data. The difference in target root mean square (RMS) error and percentage of final overlap for the iterations are fixed at 1×10^{-5}

units and 100% respectively. The cloud-to-mesh distance is analyzed for the registered scanned cloud with reference to the mesh at a fixed octree level of 6 to compute the mean and maximum error distance. A typical post-analysis error distribution histogram is shown in Figure 4. The error distance generally follows a normal distribution which is used to estimate its mean and standard deviation. The overall cloud can also be compared in a region-wise fashion using segmentation by isolating each faces of the cuboid separately to obtain finer resolution. The overlapped data can also be used as a preliminary qualification tool to analyze the error distances between the reference cloud and the scanned cloud. A lower error distance indicates better dimensional tolerance and similarity between the 3D design and the printed sample.

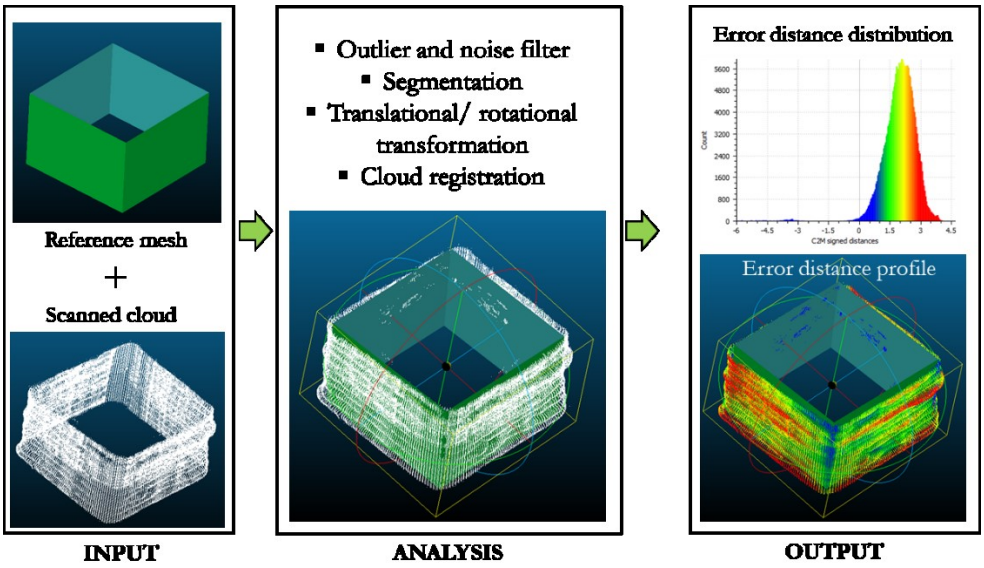

Figure 4: Process flow in using error distance distribution for post-print analysis

2.3.2 Print accuracy index based on centroidal method

The centroidal method is based on the idea of error in distance between the reference and scanned cloud based on the centroid of the aligned clouds. A schematic that illustrates the centroidal method is shown in Figure 5. The scanned cloud and reference mesh are registered with respect to the centroid. Centroidal distance is the magnitude of the vector from the centroid (the dot in the center of the figure) to a point on the scanned cloud or the reference mesh. A vector drawn from the centroid to a given point of interest on the scanned cloud (dot on the face of the cube) is shown with a magnitude of 'd_{cs}'. The vector is extended to the reference mesh to measure the incremental distance 'Δ' which signifies the error in mismatch.

The ratio of distance from the centroid to the scanned cloud (d_{cs}) over the distance from the centroid to the reference mesh (D_{cr}) is cumulatively averaged for 'n' points in the cloud, to define a print accuracy index (PAI) given by:

$$PAI = \frac{\sum_{i=1}^{n} \frac{d_{cs\ (\text{centroid} \rightarrow \text{point on the scanned cloud})}}{D_{cr\ (\text{centroid} \rightarrow \text{extrapolated point on the reference mesh})}}}{n} \quad \text{Eq. 1}$$

This ratio for a typical point in the scanned cloud is an indication of the position of the point with respect to the reference cloud. A PAI value greater than 1.0 implies that the actual point is outside the reference cloud's bounds, and vice-versa. Note that tangential extrapolation is used for the calculation, and the normal vector to the points in the scanned cloud are not considered for nearest point calculation. A similar procedure has been established in another work, which reported the comparison in terms of the Hausdorff distance to calculate an output quality index [34]. The centroidal method algorithm is employed in a MATLAB environment that takes in the input and reference cloud data, and provides a single value that can be used as a first-order quantifier to assess the print accuracy.

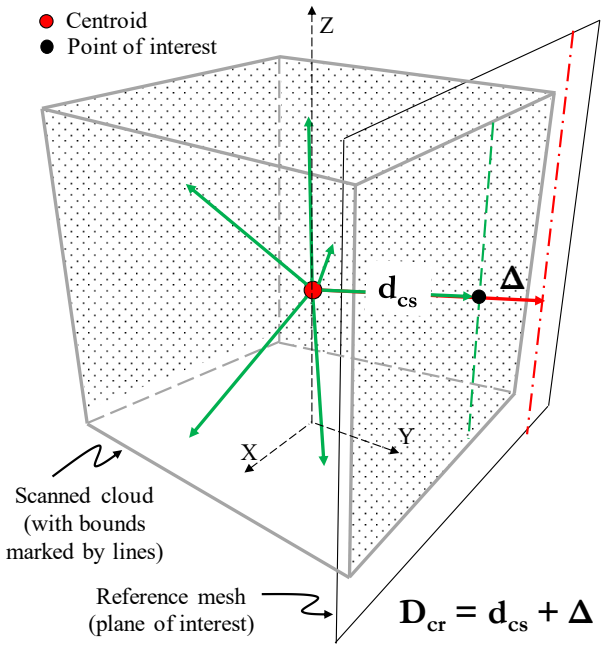

Figure 5: Schematic showing the centroidal method with the registered scanned cloud overlapped with the reference mesh.

2.4 Topological set theory analysis

The centroidal method gives an average point cloud mismatch quantifier, which is easier for global evaluation of printability. However, for an in-depth analysis using an in-line scanning procedure or analysis with respect to the buildable height, a segmental cloud matching algorithm is required, which is accomplished in this work by utilizing elements of topological set theory (TST). This method is based on the physical overlap of segmented clouds to a specified octree level and a tolerable error in overlap [27]. Figure 6 shows the relationship between a pair of point sets (points(x) → points(y)) and the selected relations used in the point cloud comparison algorithm employed in this paper [36]. Depending on the overlap conditions, points(x) is categorized as equal, not-equal, inside, outside, overlays, or neighbor to points(y) (shown to the left) while these are translated in terms of the reference and scanned cloud points (shown to the right) in Figure 6. However, the necessary condition that is used for cloud comparison is the overlapping bounds of points from different clouds as shown within boxes in the figure. If the bounding boxes around two different set of points overlap, the mismatch is considered negligible while distant bounding boxes signify a definite mismatch.

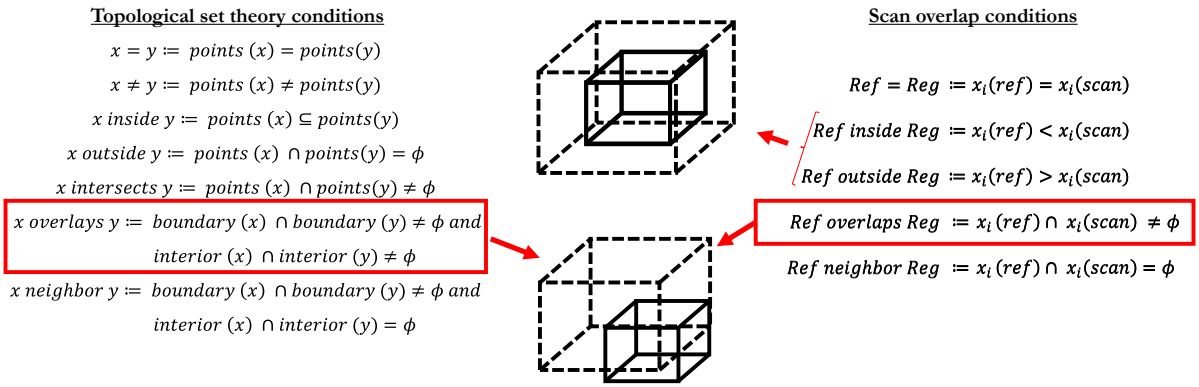

Figure 6: The topological set theory instances used in point cloud comparison. The general conditions in the set theory is shown to the left while the necessary conditions selected for analysis is shown to the right. Points(x) and points(y) corresponds to two different set of points in comparison while x_i (ref) and x_i (scan) corresponds to the boundary coordintes of bounding boxes around set of points in the reference and registered clouds respectively, where i = 1,2,3 corresponds to the 3 orthogal directions.

The TST analysis algorithm is implemented in a custom-made MATLAB program which takes in the reference and scanned cloud data as cartesian coordinate inputs. The process flow is shown in Figure 7. The scanned cloud is subjected to coarse and fine alignment transformations using Cloudcompare™ and the aligned clouds are exported in the standard point cloud data format. The Z-directional coordinates are transformed such that the minimum values of Z lie in the Z = 0 plane. In this way, the output is aligned with

the original print base as a necessary boundary condition, and the point cloud is easy to interpret with respect to the magnitude and direction from the base (where printing started) to subsequent layers (as the printing progresses). The registered cloud data is binned to the n^{th} level using an octree binning algorithm to subdivide the point cloud volume into discrete bounding elements [37]. This data is stored in a structure variable with hierarchical variables that define the octree element's bounds and the number of points held by the element. The level of octree binning is similar for both the clouds which results in the same number of bin elements (2^{3n} bin elements per n^{th} level). The k^{th} level octree bin data is isolated for further analysis. This depends on the size of the scan and the resolution in the analysis that is desired. This work considers bins in an octree level of 6 to be sufficient for the analysis. A lower 'k' value will result in an approximation of data and loss of detail in the analysis. The octree bins from the k^{th} level are sorted with respect to the height for a layer-wise comparison of the scans. Each layer may also be subdivided based on the overall height, layer height, and the octree binning level. TST is applied to identify and index the overlapping and non-overlapping octree bins. The TST method here identifies the total number of elements and the overlapping elements per layer or height step that is defined by the user. The percent overlap is calculated as the ratio of number of overlapping bins to the total number of bins in each level. A tolerable overlap for individual bins could be defined based on the level of conformance with the design model expected for print output. This user-defined measure allows for degrees of quality control with respect to the profile, for the printed element depending on the type of application. In this study, a threshold overlap condition is not defined explicitly, and a binary condition on the overlap (whether overlapping or not) is used for comparison of print quality, since this measure was found to work well as can be seen in a forthcoming section.

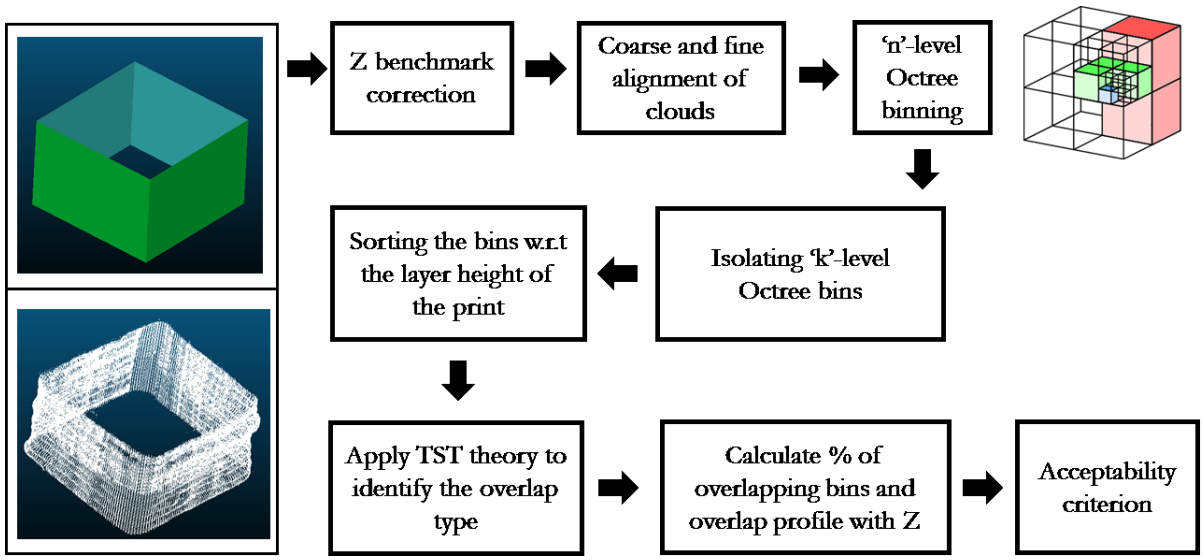

Figure 7: Steps in the implementation of the TST algorithm for post-print analysis using octree division binning and overlap check. The acceptability comparison is based on the tolerable overlap input by the user.

3 Results and Discussion

3.1 Average and maximum error distances of scanned clouds

The error distance profiles indicating the level of mismatch of a point with respect to the reference can be used as a rapid post-print qualification tool. Figure 8 shows a typical post-processed scanned cloud in comparison with the reference cloud. The overlaid clouds and the error distance profile are shown in Figure 8(a). The color jet shows the absolute error distance profile of the scanned cloud with respect to the reference cloud. The red color in Figure 8(a) indicates points that are at a higher distance from the reference cloud. Due to the corrugations on the surface resulting from the outward flow of paste through the circular nozzle, and the enlargement in the projected distances when layers are overlaid, the convex edges are mostly highlighted red while the layer interfaces are closer to the reference cloud, as expected. Figures 8(b) and (c) show the plan and side views indicating the base plane alignment used as a necessary boundary condition. The degrees of freedom in the iterative alignment were allowed only for translation in X and Y directions, and rotation around Z axis. Figure 8(d) shows the histogram of the error distances, fitted with a Gaussian distribution to extract the mean and standard deviation. The value corresponding to a 99% confidence interval is considered as an estimated maximum error distance in this work, while the mean of the Gaussian distribution can also be used as a single-value quantifier for print output quality.

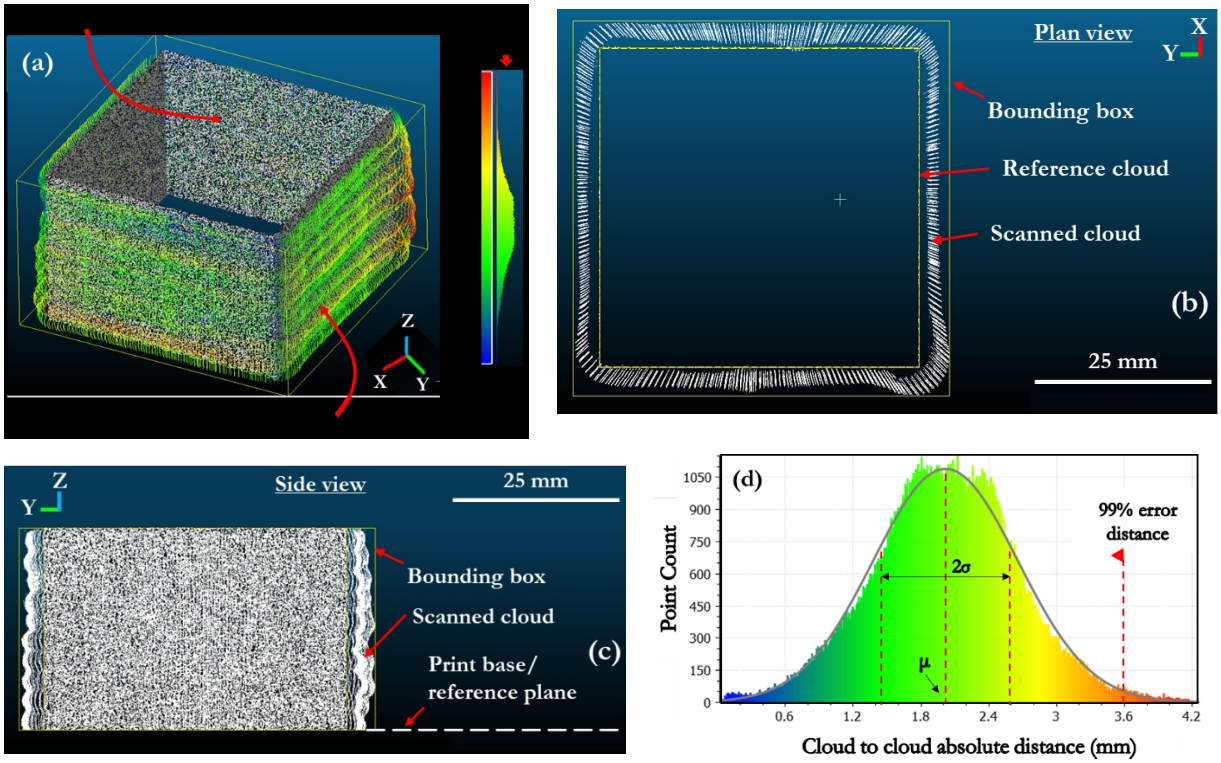

Figure 8: Images from cloud registration showing: (a) scanned cloud transformed and registered in position with the reference cloud and colorjet indicating the cloud to cloud distance, (b) plan view of the cloud with the dotted reference cloud and scanned clouds along the global bounding box, (c) the side view showing the alignment along the print base prior to registration, and (d) the error distance profile represented as a histogram and overlaid with a gaussain distribution to estimate the mean and standard deviation of the error distance along with the 99% error distance for comparison.

The spread of the distribution indicated by its standard deviation is a function of the width of the cloud surface (see the cloud in Figure 8(b); which depends on the nozzle size and chosen filament width). The maximum distance corresponds to the farthest points in the concave surface of the layers formed by the rounding of filament at the boundaries. The maximum distance could also correspond to the corners where the scanned points would be at the maximum distance from the reference cloud, provided the outliers have been removed, and only minimally influences the analysis. With the statistical parameters defined, it is also convenient to visually qualify defects or the effects of erroneous printing behavior. Although Figure 8(a) does not show too many visible error regions (red colored regions), it is because of a higher threshold error distance for the scalar fields shown. When the threshold is set close to the mean of the error distribution, as is shown in Figure 9, noticeable defects are visible including local print gaps and over-feed filaments. The

corner of the print where the print path changes is prone to a higher error because of abrupt changes in filament shape at the corners that results in a distorted shape, to maintain the flow rate. There is extra material deposition during the loop completion, which also results in print distortion. A close-up of the scanned surface (Figure 9(b)) shows the convex outer profile of the filament near its center, and a sharper joint at the inter-layer interface. The point clouds are expected to have the largest number of points in between these bounds, while local maxima could appear corresponding to the bounds as explained later.

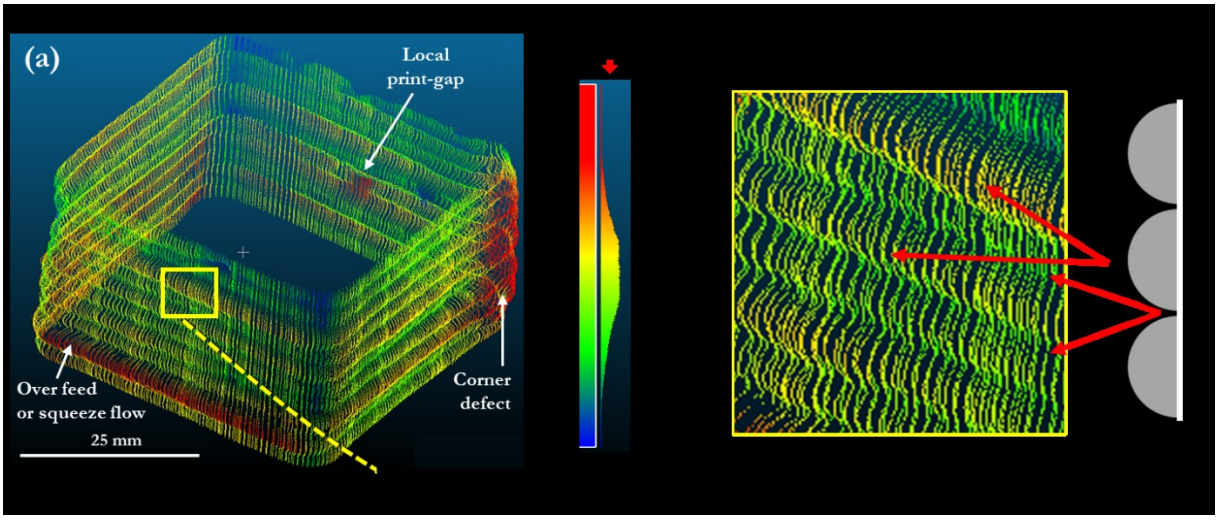

Figure 9: Typical scanned clouds showing: (a) the scalar field for cloud-to-cloud error distance with a reduced upper threshold value (set closer to the average of the gaussian distribution), showing specific regions of defects, and (b) close-up of a profile showing the rounding of filament surface.

Figure 10 shows the error distance distribution for the scanned clouds, separated for mixtures with or without superplasticizer (SP and non-SP mixtures respectively). The presence of superplasticizer enables the use of a reduced water-to-powder ratio in the mixtures, and also improves the mixture consistency. As can be noticed from Table 2, the rheology of the mixtures, and hence the buildability, which is captured indirectly by the point clouds, will be also influenced by the presence of superplasticizers. The PLA and the deltabot print data are included for comparisons in this figure, even though the details of the printer and the print process are different from those of the ram-extruded cementitious pastes. The distance data was split into 256 bins with a step value between 0.015 and 0.017 mm. Figures 10(a) and 10(c) show the error distance and probability of error in the scanned clouds for non-SP and SP mixtures respectively. The overall mean and spread of the distribution do not show visible differences between the two, even though the probability of error is higher for the non-SP mixtures. The mean error distance from the scans corresponding to the ram-extruded mixtures are generally shifted to the right of the PLA and delta print mixtures, showing

that the ram-extruded prints show a relatively higher error. Some cases show points of inflection below and above the most probable error (around the central peak) which is a characteristic of the farthest outer and inner points of the rounded filament (cluster of points appearing due to the curvature and sharp edge of the profile in each layer, as shown in Figure 9(b)).

An alternate analysis can be derived using the cumulative error distribution as shown in Figures 10(b) and 10(d). A shift in the distribution to the right shows a larger deviation from the original design surface. Typically, the graphs converge and are close (typically within the range of 1.5-2.0 mm error distance). However, larger errors are indicative of the differences in output quality of the print. The PLA print shows the least deviation while the others show errors that are approximately 4 times higher than that of the PLA print. This is due to the uniqueness in the PLA print - rheology being markedly different from that of the cement-based pastes, and the small layer thickness and flow diameter resulting in smaller and more organized layers. For the cementitious pastes, the outward flow of the material under a higher layer width influences the tolerance. The L_{30} deltabot-printed mixture has a relatively lower error distribution when compared to the other paste prints, which is an indication of better flow control in a screw-extrusion process. The $L_{15}M_{15}$ paste shows a better profile due to its finer particle packing in the presence of microsilica. The $L_{20}M_{10}$ paste consistently shows a higher error distance, specifically at the higher end of the profile. With the addition of the superplasticizer, the water demand for the otherwise finer particle distribution is limited and a better rheological flow and extrusion behavior is obtained [5,38]. This results in an overall shift of the cumulative distributions to the left as seen in Figure 10(d). Figure 10(e) shows the absolute average error distances with the standard deviation (spread of the error) and the maximum error for a confidence level of 99%. The maximum error distances are lower for the SP mixtures as shown in Figure 10(e). The average error is generally in between 1.8-2.1 mm with a spread of $\pm$0.58-0.72 mm for the ram-extruded prints, while it is 1.7 mm for the deltabot prints with a spread of $\pm$0.6 mm. The PLA printed specimen shows the smallest average error of around 0.3 mm; while the reason for such low errors were described earlier, the observed error is also attributed to thermal effects (warping while printing) which is within the typical tolerable error of around 5% of the overall dimension for PLA filaments [39,40]. The collapsed specimen shows a significantly larger error, unsurprisingly, of around 8-12 mm. The average error in this case was around 2.8 mm which indicates that the print accuracy should not be read solely in terms of the average error distance. The standard deviation was a high value of 2.7 mm, along with a cumulative spread that was shifted well to the right, which indicates an unacceptable print quality.

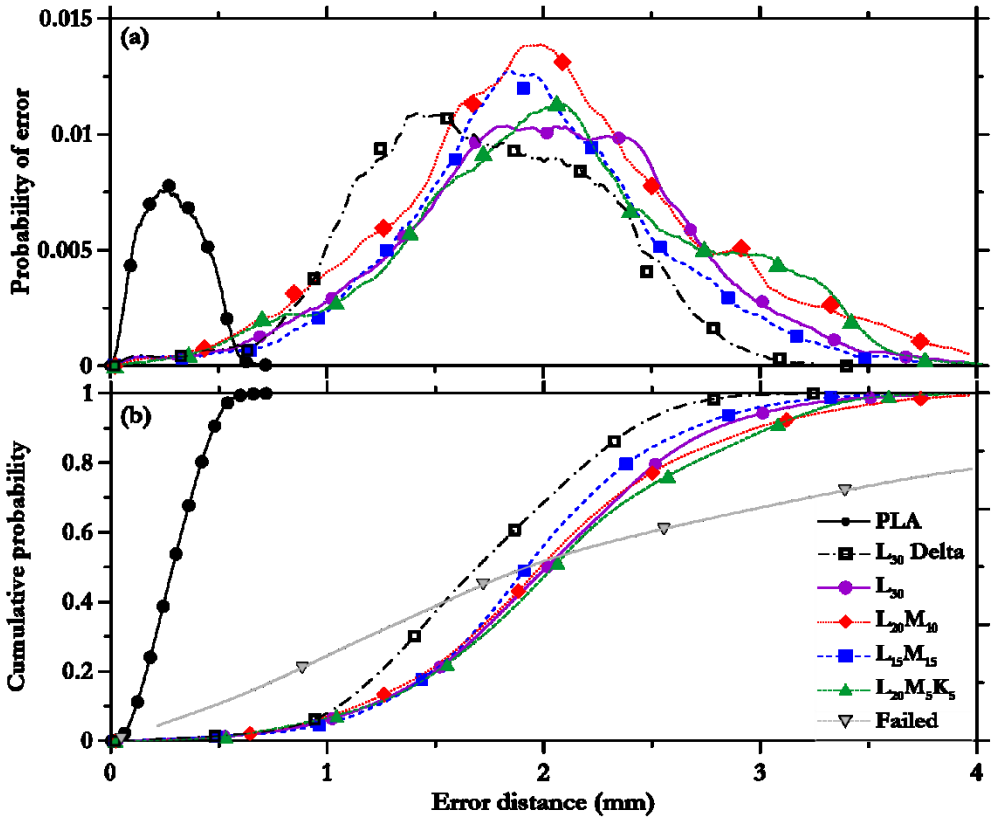
(a)
(b)
Probability of error
Cumulative probability
Error distance (mm)
0.015
0.01
0.005
0
1
0.8
0.6
0.4
0.2
0
0
1
2
3
4
PLA
L30 Delta
L30
L20M10
L15M15
L20M5K5
Failed

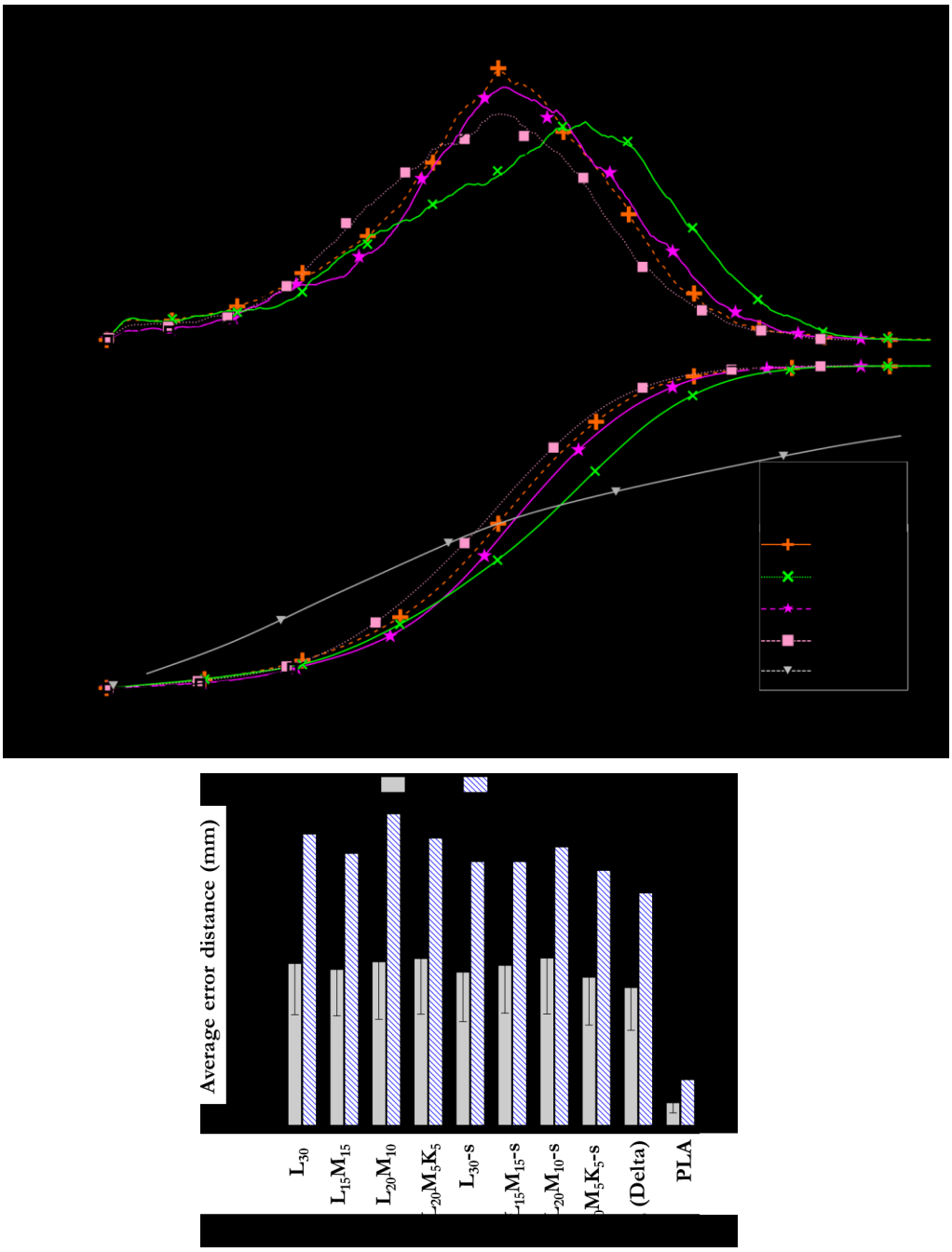

Figure 10: Cloud-to-cloud error distance analysis showing: (a-b) discrete and cumulative error distribution for non-SP mixtures, (c-d) discrete and cumulative error distribution for SP mixtures, and (e) average, standard deviation, and 99% maximum error distances for all the mixtures. PLA print is shown as the same in all the figures since it does not belong to the SP or non-SP mixtures.

3.2 Print accuracy index (PAI) and relationship with average error distance

The error distance analysis explained in the previous section provides just a single quantifiable parameter that describes whether the overall print is acceptable or not. The centroidal method defined in an earlier section can be used to generate the print accuracy index (PAI), which is shown in Figure 11. PAI close to 1.0 indicates a scanned cloud that is very close to the reference cloud. This index can be used to compare between different prints. A PAI is deemed acceptable if the average mismatch of the scanned cloud with the reference cloud is reasonable within a user-defined tolerance limit. Figure 11(a) shows the PAIs extracted using the method as detailed in the previous sections. It is found that the PAIs for the prints are generally about 1.08 to 1.09, which indicates that the prints are generally slightly larger than the designed model, and that the error distances are within 8-9% of the overall dimensions. In this case, for a 22.5 mm envelope around the centroid (45 mm length and width of the cuboid), the error distance would translate to ~1.9-2.0 mm which is consistent with the observations from the error distance analysis explained earlier (see Figure 10(e)). The PLA cloud has an index of 0.975 indicative of the print's closeness to the model. The slight mismatch is due to the overall size reduction due to inward warping along the edges. The L_{30} deltabot-printed mixture has a slightly lower PAI of 1.07 as compared to the ram-extruded prints. The failed cube shows a significantly low PAI value of 0.85 because of the larger number of points well outside the reference cloud. This mixture failed due to its lack of buildability and eventually buckled at the outer faces of the cuboid. However, the average PAI is still around 0.85 because of the failed points lying close to, and sometimes coinciding with, the reference envelope. The PAI is not highly sensitive to significant visual mismatch and hence, must be used in conjunction with a higher sensitivity, i.e., of the order of 0.005. This is clear from Figure 11(b) which shows that the PAI is proportional to the average error distance despite the minor changes in PAI across the scanned clouds of different mixtures. PAI is shown to vary at the rate of 0.05 per unit change in the mean error distance, which translates to a resolution of 0.005 for 0.1 mm error distance. It is seen that PAI is not sensitive enough to distinguish between the non-SP and SP mixtures. The close correspondence between error distances and PAI indicates that either one of these parameters can be satisfactorily used in print accuracy quantification.

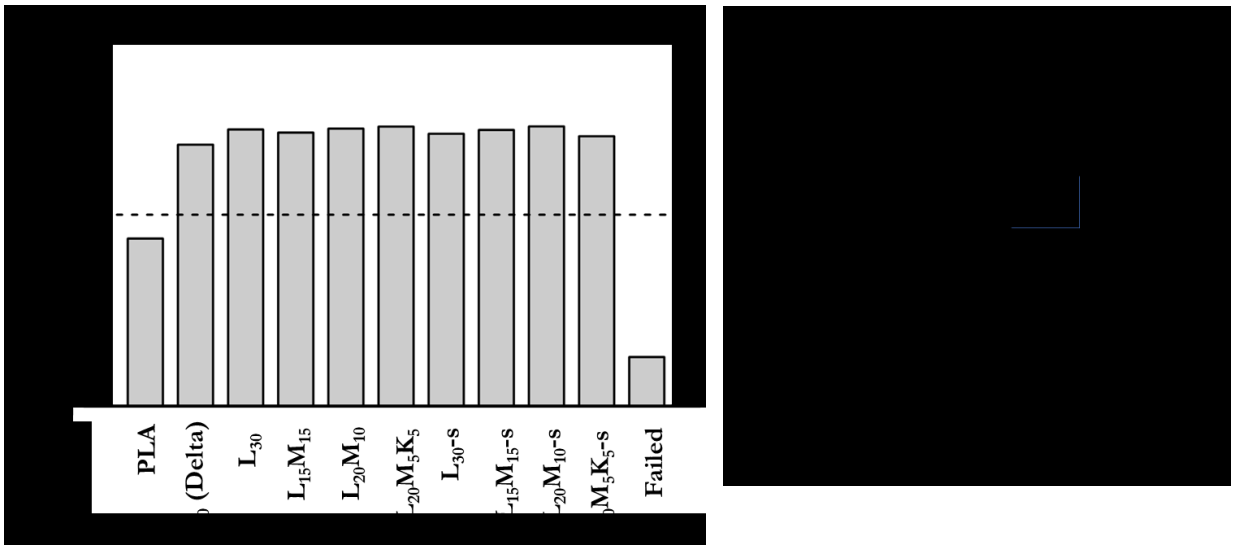

Figure 11: (a) Print accuracy index (PAI) from the centroidal method for all the prints, and (b) comparison of PAI with respect to the average error distance from the error distance analysis

3.3 Print acceptability and its variation with respect to print height using TST analysis

TST facilitates a detailed layer-wise analysis, as opposed to global analyses that were described using error distance and PAI. The method, which is dependent on the size of the input cloud data, is relatively slower and more cumbersome during the octree division stage. However, the subsequent analysis is much faster due the reduction in data units (discretization of the scanned cloud into bounding octants) that are used in the cloud comparison algorithm. This enables the overall bounding envelope to be split into finer octants. A plan view of a typical case is shown in Figure 12(a). A higher octree level (k) results in a finer division and smaller octants, increasing the accuracy of the analysis while compromising on the process speed. An octree level of 6 is used consistently for analysis within the scope of this study, and the empty octants are automatically removed after the recursive subdivision. As shown in Figure 12(a), the non-empty finer octants are predominantly clustered near the outer edges of the bounding envelope where the scanned points are mostly concentrated (see Figure 12(a)). Since a k^{th} level octree outputs 2^{3k} bounding elements, the empty octants (mostly near the centroidal Z-axis) are omitted in the analysis. The bounding elements are checked for overlap within a geometric tolerance of 3 mm from the reference point cloud (or design surface) and assigned a binary unit of 0 or 1 corresponding to no-overlap or overlapped cases respectively. In this case, a tolerable overlap has been considered for any octree bins overlapping within 45 ± 3 mm where 45 mm is the length and width of the print design and 3 mm corresponds to half the filament width.

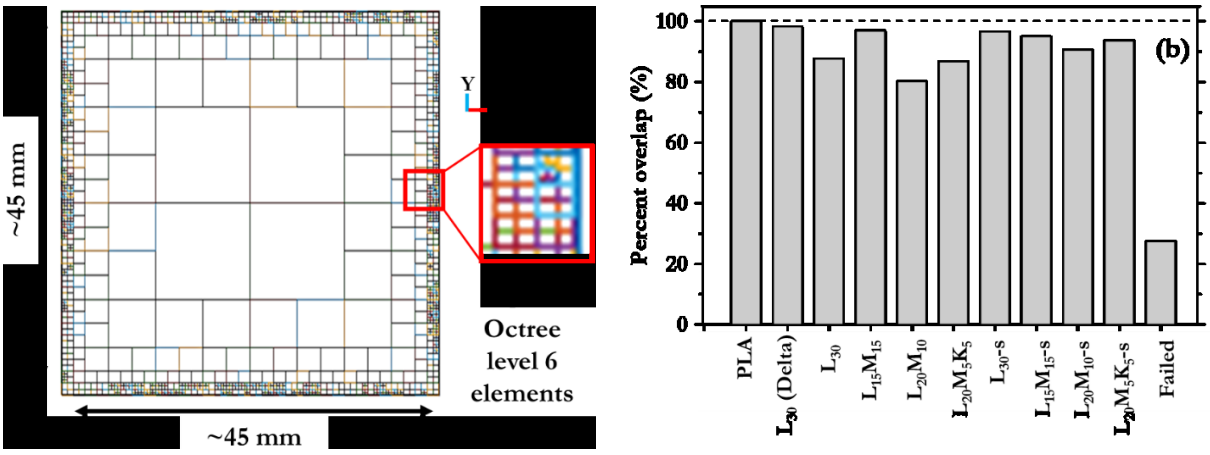

Figure 12: TST analysis output showing (a) a plan view of the octree division of the bounding box around the scanned cloud wherein the octree6 elements are used for overlap check and analysis, and (b) the average precent overlap evaluated using the TST analysis.

The ratio of the number of overlapping cases to the total number of non-empty octree-6 elements gives the total percentage overlap as shown in Figure 12(b). The average percent overlap is between 80-100% for all the scanned clouds in this study, except for the failed print. Physically, this signifies the percentage of the scanned surface that is overlapping with the design envelope while the difference corresponds to regions in the print where local failures (overburden pressure or buckling) or inadequate material flow (underflow or overflow) occurs. The sensitivity of the percent overlap to the type of mixture is relatively higher (more variability noticed in percent overlap than in PAI or mean error distance), and thus, this parameter is more physically relatable as a print qualification/quantification criterion. The PLA print output shows a 100% overlap while the deltabot-printed specimen shows an overlap close to 98% (likely due to minor mismatches observed in the topmost layers) as seen in Figure 12. A detailed analysis of the overlap is further possible in terms of the print height (or layers) by plotting the average octant overlap with respect to the height as shown in Figure 13. A 100% overlap for all the layers is the ideal scenario which is observed in the case of a PLA print (Figure 13(a)), while most of the prints show an 80-100% overlap which varies across the layer height. With minor flaws in a few layers, the deltabot-printed specimen showed better output quality when compared to the ram-extrusion based prints, because of better control during screw extrusion. The SP mixtures tend to deviate less from the target geometric tolerance when compared to the non-SP mixtures, as shown in Figure 13, because of the better printability of such mixtures. It has been shown that pastes made with a lower water-to-powder ratio, augmented by the use of SP, enables better shape retention [38]. It is also possible to enhance the printability and thus the tolerance levels using improved mixture

proportioning for the non-SP mixtures. The binary and ternary blended mixtures (containing cement and more than one replacement material) used here are based on such an idea, but further mixture modifications can likely enhance the overlap profile, and thus the tolerance. The failed cube shows a very low overall percent overlap and enhanced scatter along the height, and hence is not shown in Figure 13.

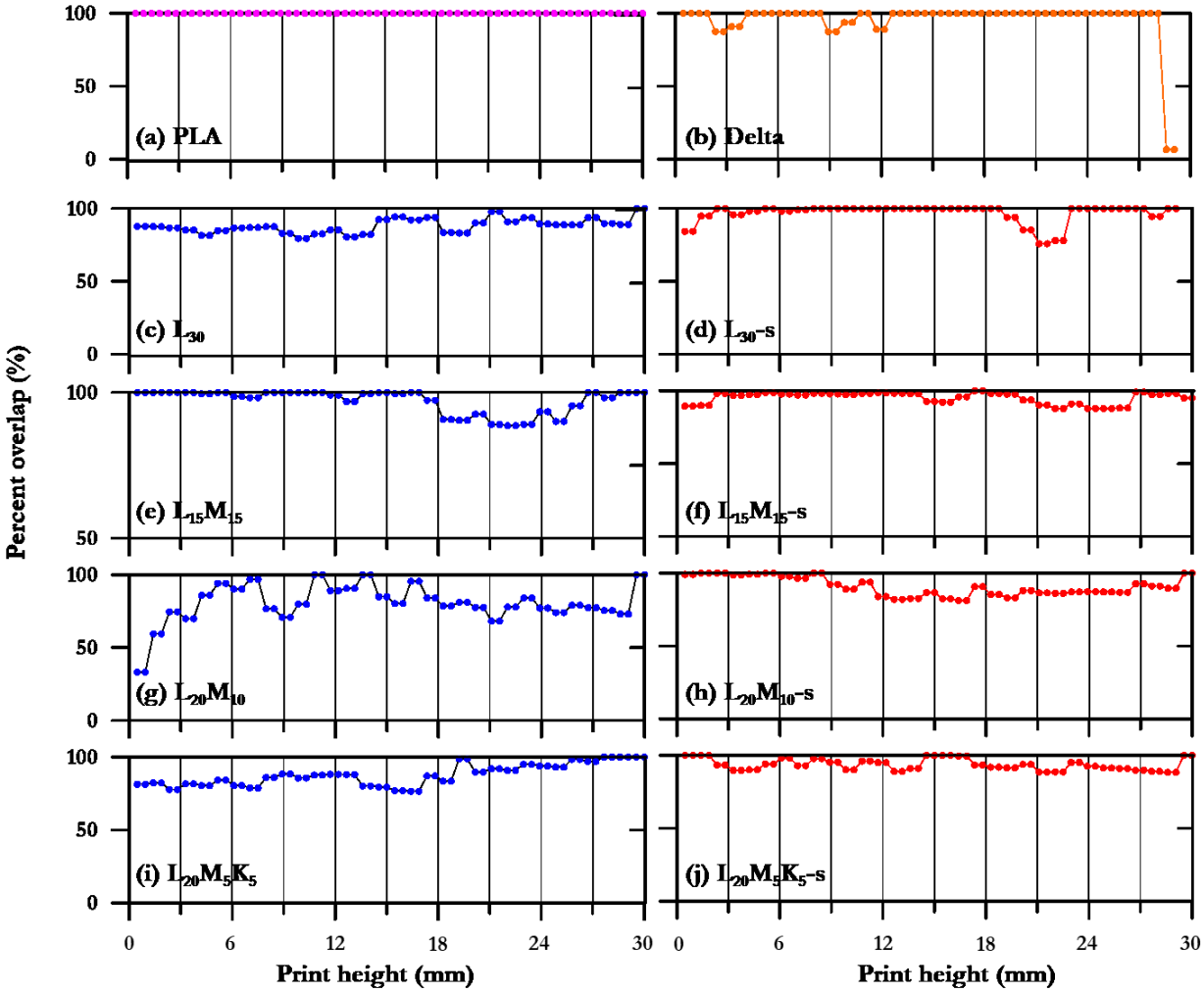

Figure 13: Overlap profile with respect to the print height estimated from TST method for the scanned clouds for: (a-b) PLA and deltabot prints, and (c-j) limestone-based pastes. Plots to the left (in blue) are the mixtures without superplasticizer (SP) and to the right (in red) are the corresponding SP mixtures.

The specific 3 mm steps (height of a single layer) showing a deviation from 100% (in the case of Figure 13) indicates a local or global flaw that has occurred in the specific layer. Thus, developing real-time layer-based overlap profiles can help identify defects during filament placing (i.e., printing). As an example,

Figure 14 shows a few cases with the point clouds imported and analyzed in Cloudcompare™. The red arrows in the image indicate local features that cause the percent overlap in the TST method (shown in Figure 13) to deviate from close to 100%. Figure 13(d) shows a lower overlap near layers 7 and 8 due to the local bulge in a filament stretch, which is visually demonstrated in Figure 14(a). A few scans show lower percent overlap in the lower layers (Figure 13(c), 13(g), and 13(i)), which can be attributed to the overburden-induced expansion of the bottom layers, which results in them becoming wider while the top layers approach 100% overlap. This is clearly shown in Figure 14(b). In contrast, a few printed specimens show lower percent overlap in the upper layers (Figure 13(h)), which likely indicates slight offset in print paths, which exacerbates as the number of layers increases, as shown in Figure 14(c). It is thus shown that the TST method applied to an octree-divided point cloud can estimate the local changes in surface profile or overall quality of print with respect to the height or time of print. This is especially advantageous as an in-line quality control check, and can be used to dynamically adjust the material or process parameters to ensure a quality print. Layered systems could be better evaluated in segments as the printing progresses. Further progress on enhancing imaging speeds and faster analysis algorithms could bring this powerful method to the mainstream, as a versatile in-line print quality analysis tool for 3D printed elements.

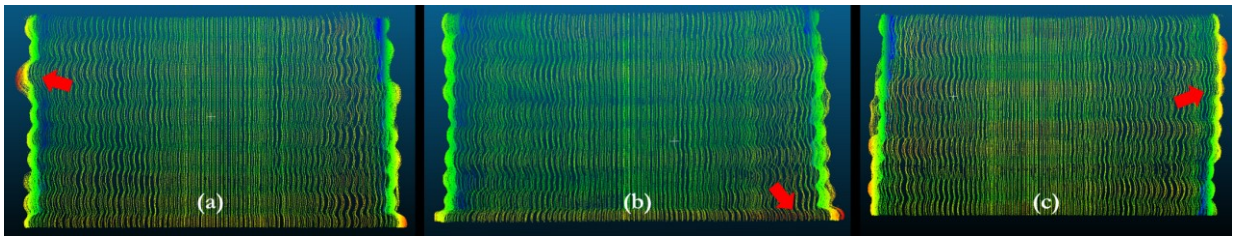

Figure 14: Point clouds from Cloudcompare™ showing defects, which accurately show up in the layer analysis in the TST method for: (a) L_{30}-s (b) $L_{20}M_{10}$-s, and (c) $L_{20}M_{10}$ mixtures. The arrows indicate the features that cause a reduction in the percent overlap with the reference cloud.

3.4 Scaled-up model and validation

The methods established were validated using a scaled-up 3D printed model using a limestone-based mortar (L_{30}-s, with 35% medium sand by volume of the mortar), printed using a gantry printer [41]. The printed specimen (cylinder; 150 mm in diameter and 600 mm high) and the scanning setup are shown in Figure 15(a). A handheld scanner (3DSystems Sense™) with a resolution of 0.9 mm, capable of scanning objects up to 3 m (size in orthogonal directions) was used to generate the output scanned object. Fine details below 0.9 mm may not be appropriately captured by this setup, but it is anticipated to be sufficient to demonstrate the efficacy of the approach for the chosen size of the scanned specimen. Figure 15(b) shows the finished

output from the scan after post-processing, with the region of interest marked (red outline). The external regions are removed and noise is filtered using Cloudcompare™. The mesh data is used to sample the cloud of 500,000 points for further analysis. Figure 15(c) shows the error distance profile from the visual analysis showing an average error distance of 5.5 mm and a standard deviation of 2.60 mm. This corresponds to approximately 3.67% error for the 150 mm diameter specimen, and is consistent with the cuboidal scan results which showed around 4.4% error (average error around 2 mm for 45 mm length). The outward flow of filaments (the layer width being larger than the nozzle size, and the effect of overburden pressure for the lower layers) and the rounding of edges results in an average error of less than 5%. Majority of the mismatch is observed near the bottom layers (error regions in the upper end of the scale) which is attributed to deformations from the overburden pressure. The PAI is 1.069 for this case, which is also in the lower end of the observed indices as discussed earlier. The corresponding TST output is shown in Figure 15(c) which shows higher local deformations in the bottom layers, while the percent overlap is close to perfect (an average global overlap of 99%) beyond 12 layers. The information shown here is a proof-of-concept in using the error distance and TST approach in macroscale 3D-printed specimens to execute the post-print quality check in a discretized and speedy manner. The size of the scan envelope and the scanner specifications will influence the output and thus the decisions arrived at. This aspect needs to be further evaluated, with an emphasis on scanner selection and defining the process in a large-scale construction setting.

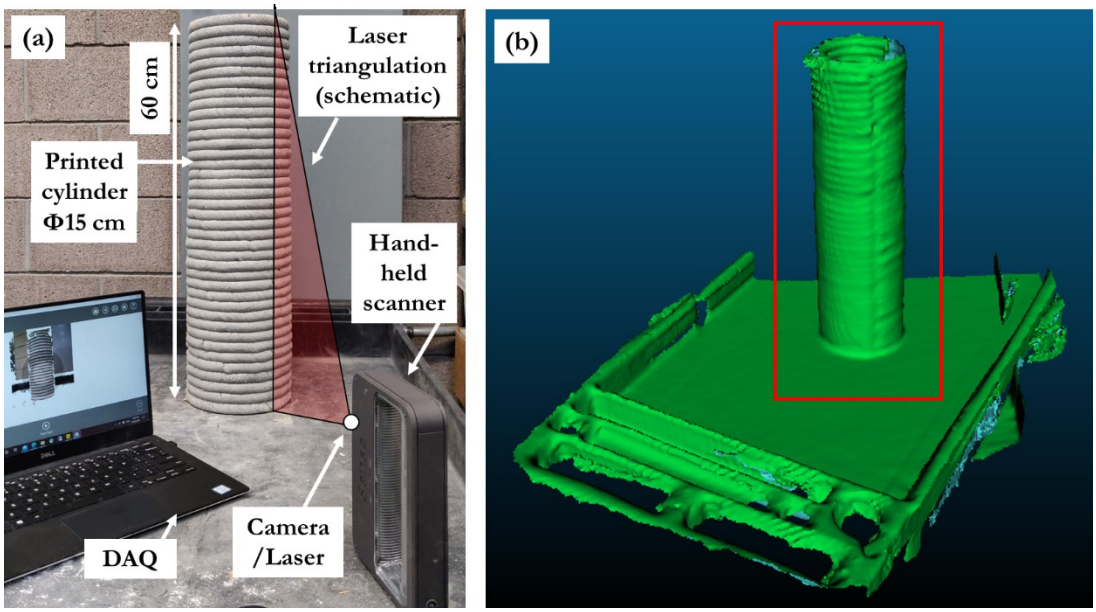

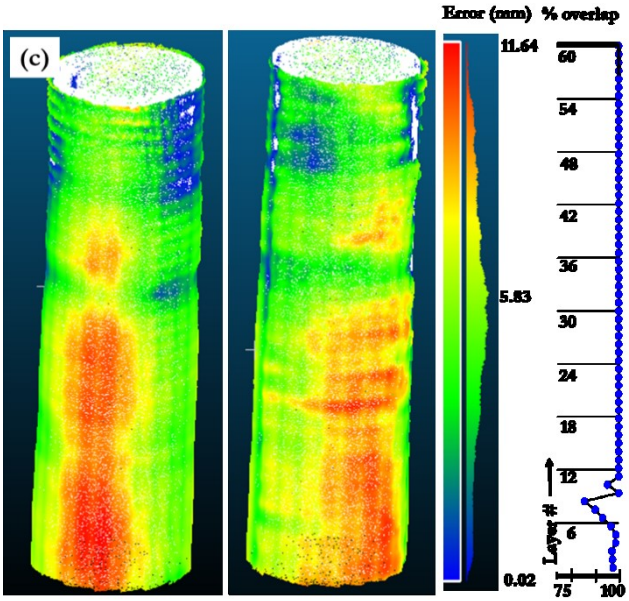

Figure 15: (a) Cylindrical printed specimens used for scaled-up scanning validation showing the dimensions and components of the setup, (b) scanned object after meshing and exported as 3D object (.stl/.obj) format, and (c) visual error distance profiles extracted using Cloudcompare© with the global error distribution and layer-wise TST profile shown for comparison. The distances are shown in cm in the percent overlap, while it is in mm in the error distance color map.

3.5 Proposed quality assessment protocol: Some comments to guide selection

The benefits and limitations of each of the aforementioned techniques have to be evaluated carefully before arriving at an appropriate quality evaluation tool. The error distance analysis is an easy tool for a layman to identify error/inconsistency hotspots in a printed specimen, and rectify them in a fast manner. However, this is a visual qualification, and the output could depend from person-to-person unless a rubric on the average and maximum mismatch is provided. Hence this method is, at best, a semi-quantitative method. Centroidal method (that defines PAI) in association with visual analysis can therefore serve as a composite quantifier to decide if a printed structure passes the geometric tolerance set beforehand. PAI is an averaged quantity that could be disadvantageous if there are a few outliers that show large discrepancies. To avoid this bias and for a detailed layer-wise analysis, the TST analysis is proposed. The TST method implements a segmental analysis of the point cloud overlap, and is a more robust approach, though the analysis time could be longer. Here, we propose a two-level quality control protocol as shown in Figure 16, wherein the error distance analysis could be used as Level 1 qualifier. Level 2 is further classified into the simplified centroidal method for PAI on a global print scale, and a segmental TST-based analysis to understand the

layer effects and to track the mismatch with respect to the print height. This sequence could be improved with additional data in each of the levels, and can prove to be a useful mode in evaluating the print tolerance, during or after printing.

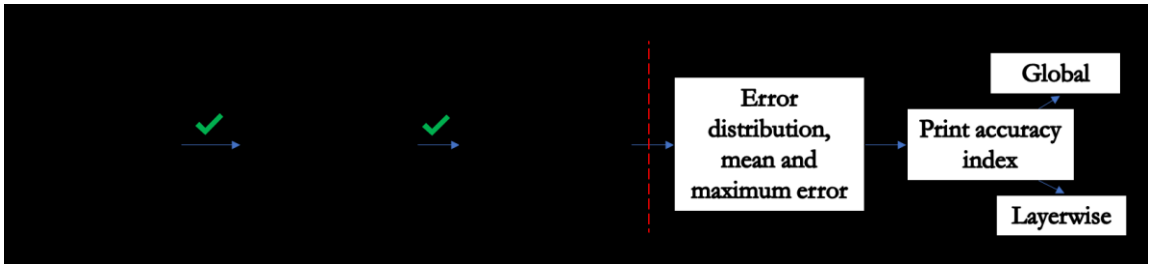

Figure 16: A two-level point cloud analysis approach to assess the print output tolerances using visual qualification, and further quantified using PAI or layer-wise TST analysis.

4 Summary and Conclusions

Evaluating the print quality in terms of the surface tolerances is important towards optimizing the process parameters and materials in 3D concrete printing. A suitably designed approach could also aid as an in-line quality control tool during the process of printing. This study describes a suite of print quality assessment protocols based on both visual qualification/quantification as well as global and layer-wise quantifiable parameters. Several small-scale printed paste specimens were subjected to 3D scanning to extract the point clouds to be used as input data for three different print quality assessment methods. These methods were used to evaluate how closely the printed specimens matched the 3D design. A visual point cloud analysis that outputs a subjective error distance profile was used as a semi-quantitative analysis method, while mathematical morphology-based approaches including the centroidal and topological set theory methods were employed for quantification of tolerances and print accuracy.

In the first (semi-quantitative) method, an error distance comparison technique that uses the best-fit registration of the reference and scanned clouds to estimate the mismatch in terms of the error distances, was used. The maximum and average error distances were used to evaluate different test-cases printed with FDM-based PLA, and cement pastes printed under screw extrusion and ram extrusion processes respectively. All the prints except the failed cuboid showed average error distances within 5% of the overall design dimension (i.e., in the range of 1.5 to 2 mm). The error distances were found to be in agreement with the print accuracy index (PAI) derived from a centroidal distance-based morphological approach. The PAI values for the printed cuboids ranged from 1.07 to 1.09. The error distances and PAIs were found to be linearly related, providing the capability to replace one with the other if sufficient calibrations are carried

out. The abovementioned methods provide the overall (global) geometrical accuracy of the print, which while being very useful, sometimes misses the critical inconsistences (if any) present at a local (layer-wise) scale. To overcome this drawback, this work used a morphological analysis method based on topological set theory (TST) that uses the octree division of the point cloud to determine the percent overlap between the scanned and reference clouds in a layer-wise manner. All the test print cases showed a global percentage overlap between 80-100% while the layer-wise overlap profile pinpoints localized inconsistencies in printing, either due to material property variations, process changes, or layer misalignment (print path changes). Deformation of the lower layers under overburden pressure results in lower percent overlap for the lower layers, while cumulative changes in print path from layer-to-layer results in misalignment of the upper layers and consequently a lower percent overlap. The chosen methodologies were verified by printing a 150 mm diameter × 600 mm high hollow mortar column. It is suggested that the proposed techniques can be used as a two-level quality control/evaluation procedure wherein: (a) a first-level analysis is made up of global error distance distribution, which can be accomplished rather quickly, and (b) a second level analysis comprised of PAI determination (for global quantification) and/or TST approach to determine layer-wise percent overlap (for localized error detection). This approach is expected to be beneficial for both post-print and in-line quality control, to identify materials- or process-related issues during or after printing.

5 Acknowledgements

The authors sincerely acknowledge the support from U.S. National Science Foundation (CMMI: 1727445; OISE: 2020095) towards this project. The authors also acknowledge the support from Salt River Materials Group, Omya, and BASF in donating the materials, and the use of 3D printing and material characterization facilities within the Laboratory for the Science of Sustainable Infrastructural Materials (LS-SIM) at Arizona State University in the completion of this project.

6 References

[1] I. Hager, A. Golonka, R. Putanowicz, 3D Printing of Buildings and Building Components as the Future of Sustainable Construction?, Procedia Engineering. 151 (2016) 292–299. https://doi.org/10.1016/j.proeng.2016.07.357.

[2] B. Khoshnevis, D. Hwang, K.-T. Yao, Z. Yeh, Mega-scale fabrication by Contour Crafting, International Journal of Industrial and Systems Engineering. 1 (2006) 301–320. https://doi.org/10.1504/IJISE.2006.009791.

[3] R.A. Buswell, W.R. Leal de Silva, S.Z. Jones, J. Dirrenberger, 3D printing using concrete extrusion: A roadmap for research, Cement and Concrete Research. 112 (2018) 37–49. https://doi.org/10.1016/j.cemconres.2018.05.006.

[4] G. Ma, Z. Li, L. Wang, Printable properties of cementitious material containing copper tailings for extrusion based 3D printing, Construction and Building Materials. 162 (2018) 613–627. https://doi.org/10.1016/j.conbuildmat.2017.12.051.

[5] S.A. Nair, H. Alghamdi, A. Arora, I. Mehdipour, G. Sant, N. Neithalath, Linking fresh paste microstructure, rheology and extrusion characteristics of cementitious binders for 3D printing, Journal of the American Ceramic Society. 102 (2019) 3951–3964. https://doi.org/10.1111/jace.16305.

[6] V.N. Nerella, M. Krause, V. Mechtcherine, Practice-Oriented Buildability Criteria for Developing 3D-Printable Concretes in the Context of Digital Construction, (2018). https://doi.org/10.20944/preprints201808.0441.v1.

[7] J.J. Benbow, J. Bridgwater, Paste flow and extrusion, Clarendon Press, Oxford, UK, 1993.

[8] A. Perrot, D. Rangeard, Y. Melinge, P. Estelle, C. Lanos, Extrusion Criterion for Firm Cement-based Materials, Applied Rheology. 19 (2009). https://doi.org/10.3933/ApplRheol-19-53042.

[9] Q. Yuan, Z. Li, D. Zhou, T. Huang, H. Huang, D. Jiao, C. Shi, A feasible method for measuring the buildability of fresh 3D printing mortar, Construction and Building Materials. 227 (2019) 116600. https://doi.org/10.1016/j.conbuildmat.2019.07.326.

[10] E. Keita, H. Bessaies-Bey, W. Zuo, P. Belin, N. Roussel, Weak bond strength between successive layers in extrusion-based additive manufacturing: measurement and physical origin, Cement and Concrete Research. 123 (2019) 105787. https://doi.org/10.1016/j.cemconres.2019.105787.

[11] R.J.M. Wolfs, F.P. Bos, T.A.M. Salet, Hardened properties of 3D printed concrete: The influence of process parameters on interlayer adhesion, Cement and Concrete Research. 119 (2019) 132–140. https://doi.org/10.1016/j.cemconres.2019.02.017.

[12] B. Panda, C. Unluer, M.J. Tan, Investigation of the rheology and strength of geopolymer mixtures for extrusion-based 3D printing, Cement and Concrete Composites. 94 (2018) 307–314. https://doi.org/10.1016/j.cemconcomp.2018.10.002.

[13] H. Alghamdi, S.A.O. Nair, N. Neithalath, Insights into material design, extrusion rheology, and properties of 3D-printable alkali-activated fly ash-based binders, Materials & Design. 167 (2019) 107634. https://doi.org/10.1016/j.matdes.2019.107634.

[14] W.-J. Long, C. Lin, J.-L. Tao, T.-H. Ye, Y. Fang, Printability and particle packing of 3D-printable limestone calcined clay cement composites, Construction and Building Materials. 282 (2021) 122647. https://doi.org/10.1016/j.conbuildmat.2021.122647.

[15] V.N. Nerella, M. Näther, A. Iqbal, M. Butler, V. Mechtcherine, Inline quantification of extrudability of cementitious materials for digital construction, Cement and Concrete Composites. 95 (2019) 260–270. https://doi.org/10.1016/j.cemconcomp.2018.09.015.

[16] B. Panda, S. Chandra Paul, M. Jen Tan, Anisotropic mechanical performance of 3D printed fiber reinforced sustainable construction material, Materials Letters. 209 (2017) 146–149. https://doi.org/10.1016/j.matlet.2017.07.123.

[17] A.V. Rahul, M. Santhanam, Evaluating the printability of concretes containing lightweight coarse aggregates, Cement and Concrete Composites. 109 (2020) 103570. https://doi.org/10.1016/j.cemconcomp.2020.103570.

[18] G. Ma, Y. Li, L. Wang, J. Zhang, Z. Li, Real-time quantification of fresh and hardened mechanical property for 3D printing material by intellectualization with piezoelectric transducers, Construction and Building Materials. 241 (2020) 117982. https://doi.org/10.1016/j.conbuildmat.2019.117982.

[19] Inspecting manufacturing precision of 3D printed concrete parts based on geometric dimensioning and tolerancing, Automation in Construction. 117 (2020) 103233. https://doi.org/10.1016/j.autcon.2020.103233.

[20] W. Lao, M. Li, T.N. Wong, M.J. Tan, T. Tjahjowidodo, Improving surface finish quality in extrusion-based 3D concrete printing using machine learning-based extrudate geometry control, Virtual and Physical Prototyping. 15 (2020) 178–193. https://doi.org/10.1080/17452759.2020.1713580.

[21] S. Lim, R.A. Buswell, P.J. Valentine, D. Piker, S.A. Austin, X. De Kestelier, Modelling curved-layered printing paths for fabricating large-scale construction components, Additive Manufacturing. 12 (2016) 216–230. https://doi.org/10.1016/j.addma.2016.06.004.

[22] B. Khoshnevis, Automated construction by contour crafting—related robotics and information technologies, Automation in Construction. 13 (2004) 5–19. https://doi.org/10.1016/j.autcon.2003.08.012.

[23] J. Xu, L. Ding, P.E.D. Love, Digital reproduction of historical building ornamental components: From 3D scanning to 3D printing, Automation in Construction. 76 (2017) 85–96. https://doi.org/10.1016/j.autcon.2017.01.010.

[24] L. Li, F. Yu, J. Shi, S. Shen, H. Teng, J. Yang, X. Wang, Q. Jiang, In situ repair of bone and cartilage defects using 3D scanning and 3D printing, Sci Rep. 7 (2017) 9416. https://doi.org/10.1038/s41598-017-10060-3.

[25] D. Berjon, R. Pages, F. Moran, Fast feature matching for detailed point cloud generation, in: IEEE, 2016: pp. 1–6. https://doi.org/10.1109/IPTA.2016.7820978.

[26] D. Girardeau-Montaut, M. Roux, R. Marc, G. Thibault, Change detection on points cloud data acquired with a ground laser scanner, International Archives of Photogrammetry, Remote Sensing and Spatial Information Sciences. 36 (2005) W19.

[27] R. Schnabel, R. Klein, Octree-based Point-Cloud Compression, (n.d.) 11.

[28] D.P. Huttenlocher, G.A. Klanderman, W.J. Rucklidge, Comparing images using the Hausdorff distance, IEEE Transactions on Pattern Analysis and Machine Intelligence. 15 (1993) 850–863.

[29] P.J. Besl, N.D. McKay, A method for registration of 3-D shapes, IEEE Transactions on Pattern Analysis and Machine Intelligence. 14 (1992) 239–256. https://doi.org/10.1109/34.121791.

[30] A. Kazemian, X. Yuan, O. Davtalab, B. Khoshnevis, Computer vision for real-time extrusion quality monitoring and control in robotic construction, Automation in Construction. 101 (2019) 92–98. https://doi.org/10.1016/j.autcon.2019.01.022.

[31] S.A.O. Nair, S. Panda, M. Santhanam, G. Sant, N. Neithalath, A critical examination of the influence of material characteristics and extruder geometry on 3D printing of cementitious binders, Cement and Concrete Composites. 112 (2020) 103671. https://doi.org/10.1016/j.cemconcomp.2020.103671.

[32] Y.W.D. Tay, M.Y. Li, M.J. Tan, Effect of printing parameters in 3D concrete printing: Printing region and support structures, Journal of Materials Processing Technology. 271 (2019) 261–270. https://doi.org/10.1016/j.jmatprotec.2019.04.007.

[33] K. Wi, V. Suresh, K. Wang, B. Li, H. Qin, Quantifying quality of 3D printed clay objects using a 3D structured light scanning system, Additive Manufacturing. 32 (2020) 100987. https://doi.org/10.1016/j.addma.2019.100987.

[34] S. Ketel, G. Falzone, B. Wang, N. Washburn, G. Sant, A printability index for linking slurry rheology to the geometrical attributes of 3D-printed components, Cement and Concrete Composites. (2018). https://doi.org/10.1016/j.cemconcomp.2018.03.022.

[35] H.T. Afarani, W. Carroll, E.J. Garboczi, J.J. Biernacki, Designing 3D printable cementitious materials with gel-forming polymers, Construction and Building Materials. 268 (2021) 121709. https://doi.org/10.1016/j.conbuildmat.2020.121709.

[36] M.J. Egenhofer, R.D. Franzosa, Point-set topological spatial relations, International Journal of Geographical Information Systems. 5 (1991) 161–174. https://doi.org/10.1080/02693799108927841.

[37] octree - partitioning 3D points into spatial subvolumes - File Exchange - MATLAB Central, (n.d.). https://www.mathworks.com/matlabcentral/fileexchange/40732 (accessed July 12, 2018).

[38] S.A.O. Nair, N. Neithalath, Flow Characterization of 3D Printable Cementitious Pastes during Extrusion using Capillary Rheometry, ACI Materials Journal. (n.d.).

[39] Accuracies and tolerances in 3D printing, 3Faktur. (2018). https://3faktur.com/en/accuracies-and-tolerances-in-3d-printing/ (accessed April 4, 2021).

[40] Optimizing the Accuracy and Tolerance of Your 3D Printer, 3D Insider. (2020). https://3dinsider.com/3d-printing-accuracy/ (accessed April 4, 2021).

[41] S.A.O. Nair, A. Tripathi, N. Neithalath, Examining layer height effects on the flexural and fracture response of plain and fiber-reinforced 3D-printed beams, (2020).